Journal of Materials Chemistry A

PAPER

View Article Online
View Journal | View Issue

Cite this: J. Mater. Chem. A, 2019, 7, 2589

Origins of ultralow thermal conductivity in 1-2-1-4 quaternary selenides†

Jimmy Jiahong Kuo, [a] Umut Aydemir,[b] Jan-Hendrik Pöhls,[c] Fei Zhou, [d] Guodong Yu,[ef] Alireza Faghaninia, [g] Francesco Ricci,[e] Mary Anne White, [chi] Gian-Marco Rignanese, [e] Geoffroy Hautier, [e] Anubhav Jain[g] and G. Jeffrey Snyder *[a]

Received 6th October 2018
Accepted 4th January 2019

DOI: 10.1039/c8ta09660k

rsc.li/materials-a

Engineering the thermal properties in solids is important for both fundamental physics (*e.g.* electric and phonon transport) and device applications (*e.g.* thermal insulating coating, thermoelectrics). In this paper, we report low thermal transport properties of four selenide compounds ($BaAg_2SnSe_4$, $BaCu_2GeSe_4$, $BaCu_2SnSe_4$ and $SrCu_2GeSe_4$) with experimentally-measured thermal conductivity as low as 0.31 ± 0.03 W m^{-1} K^{-1} at 673 K for $BaAg_2SnSe_4$. Density functional theory calculations predict κ < 0.3 W m^{-1} K^{-1} for $BaAg_2SnSe_4$ due to scattering from weakly-bonded Ag–Ag dimers. Defect calculations suggest that achieving high hole doping levels in these materials could be challenging due to monovalent (*e.g.*, Ag) interstitials acting as hole killers, resulting in overall low electrical conductivity in these compounds.

I. Introduction

The reduction of thermal conductivity is an important concept for various applications, such as thermal barrier coatings, thermal insulation, and thermoelectric materials. While this has been previously achieved by introducing additional scattering sources (*e.g.*, grain boundary, point defects and alloying scattering),[1] electrical properties or mechanical properties can be easily compromised by these nanostructures. Searching for and understanding materials with intrinsic low thermal conductivity is therefore challenging but crucial for realizing these applications.

Several compounds with large and complex unit cells and weak bonds between atoms exhibit intrinsically low thermal conductivity, such as $Ca_9Zn_{4+x}Sb_9$,[2] Sr_3GaSb_3 (ref. 3) and $Yb_{14}MnSb_{11}$.[4] This behavior can be explained by a model developed by Cahill and Pohl,[5] in which crystal structure is related to the atomic density, and the bond strength is related to the Debye temperature estimated by the speed of sound. Experimental thermal conductivities are often compared with their glassy limits as an estimate of room for reduction. On the other hand, it is not uncommon to find materials with experimental thermal conductivity lower than their predicted glassy limits, for example WSe_2,[6] PCBM,[7,8] and SnSe,[9] referred to as ultralow thermal conductivity. To understand the overestimation by the Cahill and Pohl model, several models have been developed. Pöhls *et al.* modified the Cahill and Pohl model by using an average phonon mean speed. Furthermore, they assumed that the phonon mean free path is frequency-dependent for dynamic disordering (*i.e.*, Umklapp process)[10] and frequency-independent for static disordering.[11] The latter agrees well with the thermal conductivity of PCBM.[11] In a recent model by Agne *et al.*,[12] the thermal conductivity limit is described by a diffusion-mediated model where diffusive transport of thermal energy through the compound is considered. In general, these models modify the estimation of Debye temperature by using an average phonon mean speed over the entire Brillouin zone to explain the ultralow thermal conductivity.[11,12]

In a recent high-throughput screening,[13] the electronic properties of 48 000 inorganic compounds indicate that several quaternary transition metal chalcogenides exhibit high predicted power factors (*i.e.*, σS^2 with σ as the electrical conductivity and S as the Seebeck coefficient). From this screening, four quaternary selenides ($BaAg_2SnSe_4$, $BaCu_2SnSe_4$, $BaCu_2GeSe_4$, and $SrCu_2GeSe_4$) were revealed to exhibit high predicted power

[a]Department of Materials Science and Engineering, Northwestern University, 2220 Campus Drive, Evanston, IL-60208, USA. E-mail: jeff.snyder@northwestern.edu
[b]Department of Chemistry, Koç University, Sariyer, Istanbul, 34450, Turkey
[c]Department of Physics and Atmospheric Science, Dalhousie University, PO BOX 15000, 6310 Coburg Rd, Halifax, NS, B3H 4R2, Canada
[d]Physical and Life Sciences Directorate, Lawrence Livermore National Laboratory, Livermore, California 94550, USA
[e]Institute of Condensed Matter and Nanosciences (IMCN), Université Catholique de Louvain, Chemin des Étoiles 8, B-1348 Louvain-la-Neuve, Belgium
[f]School of Physics and Technology, Wuhan University, Wuhan 430072, China
[g]Energy Technologies Area, Lawrence Berkeley National Lab, 1 Cyclotron Rd, Berkeley, CA, USA
[h]Clean Technologies Research Institute, Dalhousie University, PO BOX 15000, 6310 Coburg Rd, Halifax, NS, B3H 4R2, Canada
[i]Department of Chemistry, Dalhousie University, PO BOX 15000, 6310 Coburg Rd, Halifax, NS, B3H 4R2, Canada

† Electronic supplementary information (ESI) available. See DOI: 10.1039/c8ta09660k

factors ($\approx$8.5–17.3 $\mu W\,cm^{-1}\,K^{-2}$ assuming a temperature of 600 K and a hole carrier concentration of 10^{20} cm^{-3} and constant relaxation time $\approx$ 10^{-14} s). Similar high thermoelectric performance was predicted by the TEDesignLab database, which uses different approaches to computationally assess the thermoelectric potential.[14] However, experimental studies revealed that the electrical conductivity is low, most likely due to a low carrier concentration,[15] and will be unlikely to match the carrier concentration assumed in the computations. To the best of our knowledge, the thermal properties of these compounds have not been reported prior to this work.

In this paper, we focus on the understanding of the thermal transport properties of these four selenides. Three quaternary selenides (except for $BaCu_2GeSe_4$) exhibited ultralow thermal conductivity in which the origins of the thermal conductivity were delineated using a combination of experimental and first-principles studies. Furthermore, we performed doping studies to enhance the electrical properties in these materials. However, based on experimental evidence and defect calculations an increase in hole carrier concentration is challenging due to Ag interstitials serving as hole killers.

II. Results and discussion

A. Crystal structure and sample purity

Four samples investigated in this study crystallize in three different space groups: (1) $BaAg_2SnSe_4$ in *I*222 (no. 23, orthorhombic), (2) $BaCu_2GeSe_4$ in $P3_121$ (no. 152, trigonal), (3) $BaCu_2SnSe_4$, and (4) $SrCu_2GeSe_4$ in *Ama*2 (no. 40, orthorhombic) as shown in Fig. 1. While Sn and Ge atoms form almost regular tetrahedral environments with Se atoms, Ag and Cu atoms have very distorted connection pattern with Se. For example, $AgSe_4$ in (1) has two short (2.565 Å) and two long (2.933 Å) Ag–Se distances with Se–Ag–Se angle attaining a maximum angle of 172.3°. Thus it can be better described as a strongly flattened tetrahedra. The $CuSe_4$ units have slightly more regular tetrahedral environments compared to Ag atoms. In these crystal structures, while $SnSe_4$ and $GeSe_4$ are not interconnected to each other (isolated), the $AgSe_4$ are corner shared, $CuSe_4$ in (2) is edge shared and in (3) and (4) are corner shared. $AgSe_4$ units in (1) and $CuSe_4$ units in (3) and (4) form a 2D layer structure, however, $CuSe_4$ units are interlinked in (2) to construct a 3D framework structure. There are direct bonding interactions between the Ag atoms (d_{Ag-Ag} = 3.21 Å) in (1) and Cu atoms (d_{Cu-Cu} = 2.62–2.70 Å) in (3) and (4). No direct Cu–Cu contact exists in the structure of (2) (*i.e.* no evidence for Cu–Cu dimers). In these structures, Ba and Sr atoms are located in the channels surrounded with eight Se atoms forming a distorted square antiprism. One of the distinctive features of these compounds is anomalously high anisotropic thermal displacement parameters observed for the Ag and Cu atoms. While this is not unusual for compounds with Ag[16] and Cu,[17] it deserves further analysis to uncover if it is directly related to the low lattice thermal conductivity observed in these materials.

Sample purities are examined by PXRD measurement for the compounds after hot pressing, as shown in Fig. 2. The results coincide with the Inorganic Crystal Structure Database (ICSD) except for few impurity peaks observed for $BaCu_2SnSe_4$ and $SrCu_2GeSe_4$, which could not be identified by XRD analysis. Although the impurities are minor, they can contribute to the thermal and electrical transport properties.

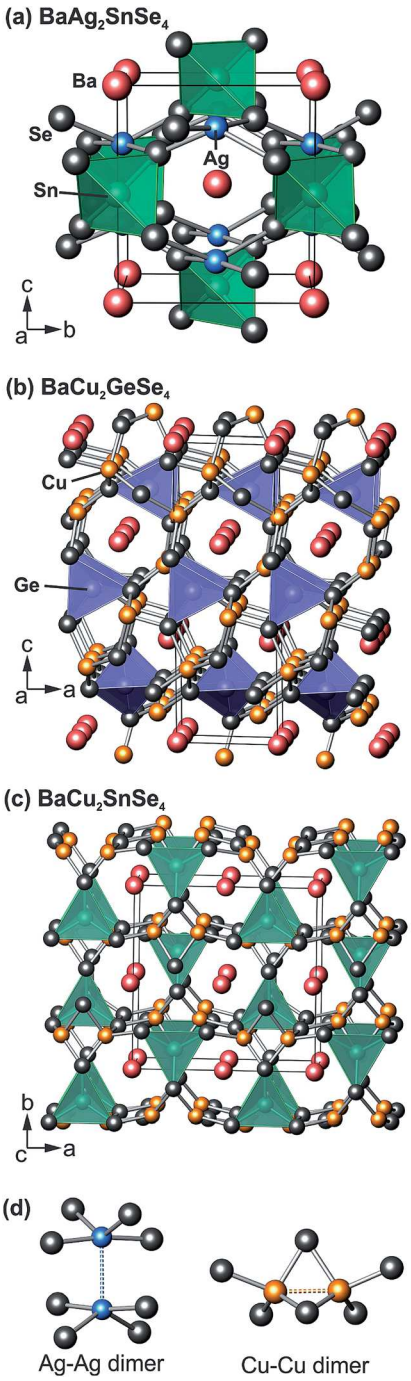

Fig. 1 Three different crystal structures among four studied selenides: (a) $BaAg_2SnSe_4$: orthorhombic *I*222 (no. 23), (b) $BaCu_2GeSe_4$: trigonal $P3_121$ (no. 152) and (c) $BaCu_2SnSe_4$: orthorhombic *Ama*2 (no. 40). $SrCu_2GeSe_4$ crystallizes in the same structure as $BaCu_2SnSe_4$. (d) Ag–Ag dimer of $BaAg_2SnSe_4$ and Cu–Cu dimers of $BaCu_2SnSe_4$ are illustrated, which act as effective phonon scattering centers to suppress lattice thermal conductivity (see Section II B for more details).

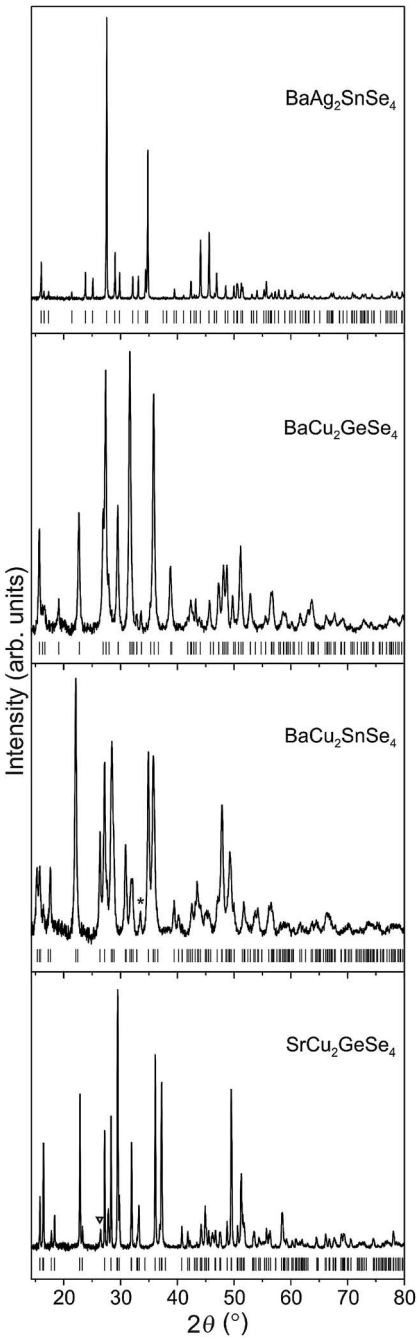

Fig. 2 PXRD pattern for the four selenide compounds. The ticks mark the calculated reflection positions of the target compounds. Samples are mostly pure in the experimental resolution except for few impurity peaks, observed near $2\theta = 33°$ in $BaCu_2SnSe_4$ and $2\theta = 27°$ in $SrCu_2GeSe_4$ as marked by a star and triangle, respectively.

B. Thermal properties

The thermal conductivity was determined using the thermal diffusivity, heat capacity, and density and is shown as a function of temperature in Fig. 3(a). The thermal conductivity can be separated into a lattice and electrical contribution. However, it is assumed that the electrical contribution to the thermal conductivity is insignificant ($\kappa_e < 0.01$ W m^{-1} K^{-1}) due to a low

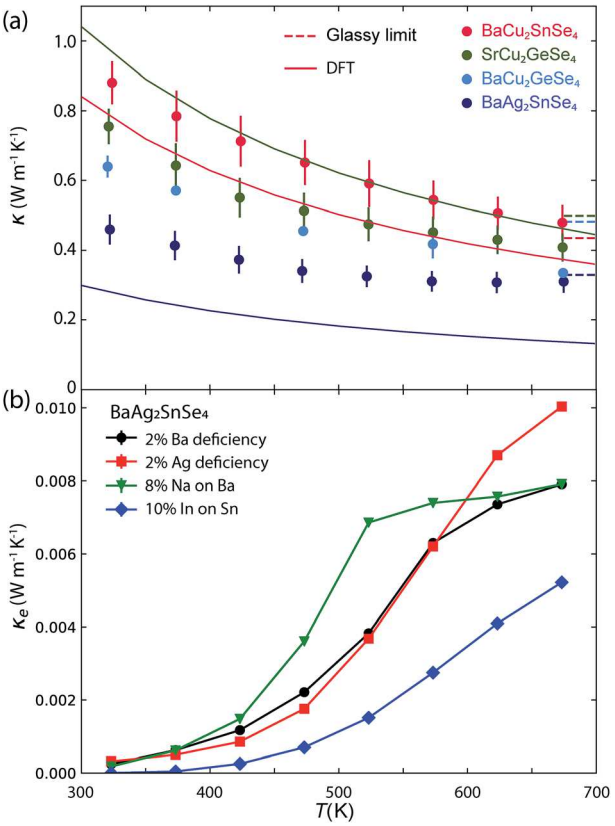

Fig. 3 (a) Experimental (dots) and theoretical thermal conductivities calculated by DFT compressed sensing method (solid lines). The dashed line segments are glassy limit predicted by Cahill's formula.[18] The computational thermal conductivity of $BaCu_2GeSe_4$ is undetermined due to a dynamic instability (see ESI†). Error bars include measurement errors of thickness, heat capacity, and diffusivity. (b) Electrical contribution to thermal conductivity is calculated using single-parabolic-band model (using data from Fig. 5). The result shows that the total thermal conductivity is dominated by the lattice contribution, therefore $\kappa \approx \kappa_L$.

electrical conductivity (Fig. 3(b)) and the thermal conductivity consists mostly of the lattice contribution. A decrease in thermal conductivity with temperature was observed for all compounds indicating that Umklapp processes are the dominant scattering mechanism.

At high temperatures, the thermal conductivity is comparable (*e.g.*, $BaCu_2SnSe_4$) and even lower (*e.g.*, $BaAg_2SnSe_4$, $BaCu_2GeSe_4$ and $SrCu_2GeSe_4$) with their predicted glassy limit.[18] In particular, $BaAg_2SnSe_4$ has extremely low thermal conductivity ($\kappa = 0.31 \pm 0.03$ W m^{-1} K^{-1} at 673 K).

Such behavior can be attributed to an overestimation of Debye temperature in the Cahill's model using speed of sounds.[11] To describe the ultralow thermal conductivity, we applied the diffusion model by Agne *et al.*[12] (Table 1). The diffusion model underestimates the experimental thermal conductivity of all studied selenides. It is important to note that while the Cahill's model dramatically overestimates the thermal conductivity of $SrCu_2GeSe_4$, the diffusion model agrees with experiments (Table 1).

Table 1 Comparison between thermal conductivity (unit: W m^{-1} K^{-1}) of Cahill's glassy limit, Agne's diffusion model and experimental high temperature limit (*i.e.*, 673 K)

Selenide	K_{Cahill}	K_{Diff}	Exp.
$BaAg_2SnSe_4$	0.31	0.24	0.31 ± 0.03
$BaCu_2SnSe_4$	0.44	0.30	0.48 ± 0.05
$BaCu_2GeSe_4$	0.50	0.34	0.41 ± 0.01
$SrCu_2GeSe_4$	0.48	0.33	0.34 ± 0.05

Table 2 Average speed of sound, V_s, coefficient of volumetric thermal expansion, α_v, heat capacity at constant pressure, C_p, and Grüneisen parameter, γ, of $BaAg_2SnSe_4$ and $BaCu_2SnSe_4$

Compounds	$BaAg_2SnSe_4$	$BaCu_2SnSe_4$
V_s (m s^{-1})	2122	2531
α_V (10^{-5} K^{-1})	3.63	4.81
C_p (J g^{-1} K^{-1})	0.25	0.33
γ	0.65	1.10

It has to be noted that the heat capacity was set to the Dulong–Petit value which can introduce uncertainty because strong anharmonicity can increase the heat capacity and hence, the thermal conductivity at elevated temperature. To verify the choice of the Dulong–Petit value, we measured the heat capacity from 2 K to 675 K (Fig. 4). At low temperature, the heat capacity increased with temperature, following by a plateau consistent with the Dulong–Petit value. Above 500 K, the heat capacity of the selenides increased with temperature most likely due to anharmonicity, whereas the heat capacity of the $BaAg_2SnSe_4$ compound remains at the Dulong–Petit value. To quantify the anharmonicity, the Grüneisen parameter was calculated (see section VI ESI†) for both Ba–Sn selenides (Table 2). Although the experimental Grüneisen parameter is low, mode-specific Grüneisen parameters, especially of the acoustic modes and the low-frequency optical modes, can contribute to the ultralow thermal conductivity in the quaternary compounds.

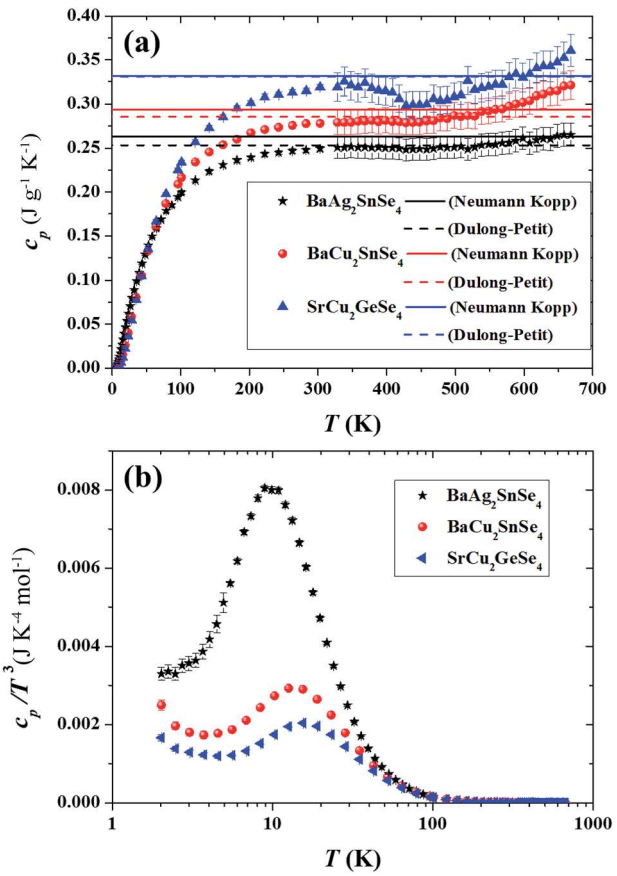

Fig. 4 (a) Experimental heat capacity of $BaCu_2SnSe_4$, $BaAg_2SnSe_4$, and $SrCu_2GeSe_4$. Heat capacity approaches the Dulong–Petit value at around 500 K, following an increase in heat capacity due to anharmonicity. $BaCu_2SnSe_4$ exhibits a higher Grüneisen parameter than $BaAg_2SnSe_4$ which is consistent with the larger anharmonic contribution of the heat capacity for $BaCu_2SnSe_4$ at high temperature. (b) Low-temperature heat capacity suggests that low-frequency optical modes suppress the acoustic modes.

The recent models for determining the thermal conductivity of ultralow thermal conductivity compounds suggest that low atomic density (N/V with N as number of atoms per unit cell and V is the volume of the unit cell) and Debye temperature are preferable. The atomic densities of the four selenides are comparable and even smaller than several compounds with low thermal conductivity, as shown in Table 3. The Debye temperature can be roughly estimated from the experimental heat capacity data by plotting C_p/T *vs.* T^2 relation, or from the phonon dispersion curves (see Fig. 6 and S2†). These results are shown in Table 4. The theoretical values of the Debye temperature are slightly lower than the values determined from experiments. Nevertheless, the Debye temperatures of $BaAg_2SnSe_4$ from both methods are even lower than for SnSe ($\theta_D = 175$ K). Note that Debye temperatures shown here can introduce uncertainties because of the lack of low-temperature heat capacity data (*i.e.*, lower than 2 K).

To further understand the origin of the ultralow thermal conductivity, density functional theory calculations were performed and the phonon dispersion curves are displayed in Fig. 6. Low-frequency optical modes can suppress the acoustic modes and hence, reduce the Debye temperature. The low-frequency optical modes are mostly due to contribution of monovalent cations (Ag^+ or Cu^+) as shown in the partial phonon density of states (pPDOS). This is, in particular, the case in $BaAg_2SnSe_4$ where the weak bonding between Ag–Ag dimers (distance 3.1 Å) gives rise to low-frequency optical modes ($\approx$0.7–1 THz). These optical modes hybridize strongly with acoustic modes and pin the transverse acoustic modes near

Table 3 Atomic density [$Å^{-3}$] of investigated selenides and other low-thermal conductivity materials

Compounds	Density	Compounds	Density
$BaAg_2SnSe_4$	0.036	Sr_3GaSb_3	0.030
$BaCu_2SnSe_4$	0.038	$Yb_{14}MnSe_{11}$	0.034
$BaCu_2GeSe_4$	0.040	Ca_9ZnSb_9	0.036
$SrCu_2GeSe_4$	0.042	SnSe	0.038

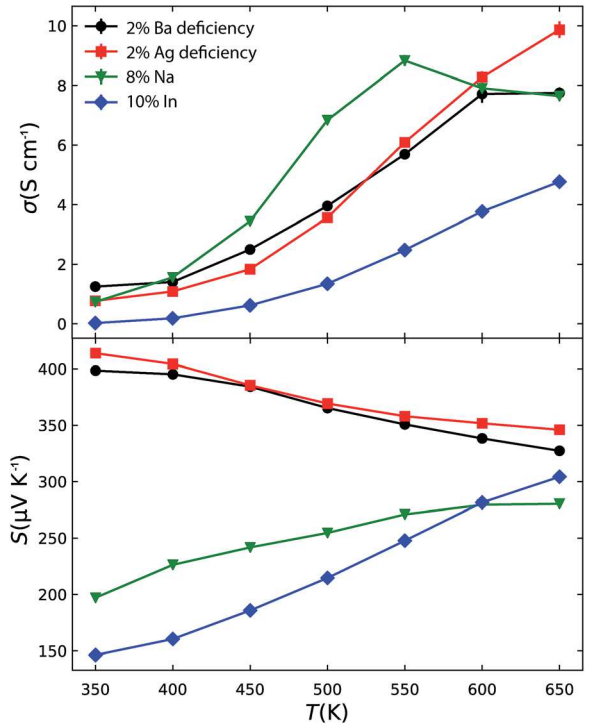

Fig. 5 Experimental measurements of electrical conductivity and Seebeck coefficient of $BaAg_2SnSe_4$-based compounds. Results include compounds with intrinsic defect (*e.g.*, Ba and Ag) as well as extrinsic dopants (*e.g.*, Na and In).

band edges to these low frequencies. As a result, the Ag partial DOS are abnormally large in the 0.7–1 THz region.

Similar to the computed phonon pDOS, the low-temperature experimental heat capacity divided by T^3 of $Ba_2AgSnSe_4$ displays a large peak (peak maximum at 10 K) suggesting low-frequency optical modes (Fig. 4). A slightly higher temperature was observed for the low-temperature peak of the heat capacity in the Cu-based selenides and the peaks were also reduced compared to that of $BaAg_2SnSe_4$. The experimental heat capacity is consistent with the phonon dispersion curves and pPDOS which show slightly higher frequencies for the Cu-based selenides (see Fig. S2 ESI†) and thus, the thermal conductivity of $BaAg_2SnSe_4$ is predicted to be lower than all three Cu-based selenides, as experimentally observed in Fig. 3.

Table 4 Experimental and theoretical Debye temperature θ_D (K) of $BaAg_2SnSe_4$, $BaCu_2SnSe_4$, and $SrCu_2GeSe_4$. Experimental θ_D is estimated by using C_p/T *vs.* T^2 relation. Theoretical θ_D is calculated from the phonon dispersion curves. θ_D of the lowest three acoustic modes are shown and the average value is calculated *via* $\theta_{D,avg}^{-3} = \sum\theta_{D,i}^{-3}/3$

Compounds	Exp. θ_D	Theo. θ_D Avg.	Mode 1	Mode 2	Mode 3
$BaAg_2SnSe_4$	160	149.6	130.5	138.4	243.8
$BaCu_2SnSe_4$	210	200.9	170.2	189.1	372.1
$SrCu_2GeSe_4$	240	195.8	154.9	204.0	428.8

The thermal conductivity was calculated using a recently-developed compressive sensing method[19] to extract higher-order force constants, which indicates good agreement with experimental results. Especially, the temperature trends of the thermal conductivity show strong correlation with the experimental thermal conductivity. The slight shift in thermal conductivity can be attributed to a slight over- or underestimation of the acoustic modes.

The low thermal conductivity of $BaAg_2SnSe_4$ shown in Fig. 3 can be attributed to the relatively small harmonic and strong anharmonic interactions of the Ag–Ag dimer. The presence of Ag–Ag dimers with low-frequency optical modes (*i.e.*, the red lines) in Fig. 6(b) leads to very low-frequency transverse acoustic modes due to hybridization between the low-energy optical and transverse acoustic modes, which are capped to 0.7 to 1 THz with reduced velocity and heat transport capabilities. This can be seen in the corresponding low-frequency partial DOS dominated by Ag contributions (Fig. 6(a), green lines). Thus, the Ag–Ag dimer can be very effective phonon scattering centers to suppress lattice thermal conductivity (see Fig. 1). Similar dimer structures with inherently low thermal conductivity can be found in other high zT thermoelectric materials (*e.g.*, Sb^{2-} dimer in Zn_4Sb_3 (ref. 20) and $Yb_{11}AlSb_9$;[21] Ga dimer in $BaGa_2Sb_2$ (ref. 22)).

C. Electrical properties and defect calculations

All four selenides studied here ($BaAg_2SnSe_4$, $BaCu_2GeSe_4$, $BaCu_2SnSe_4$ and $SrCu_2GeSe_4$), were predicted to have high power factors (*e.g.*, 8.5–17.3 μW cm^{-1} K^{-2}) if assuming a doping

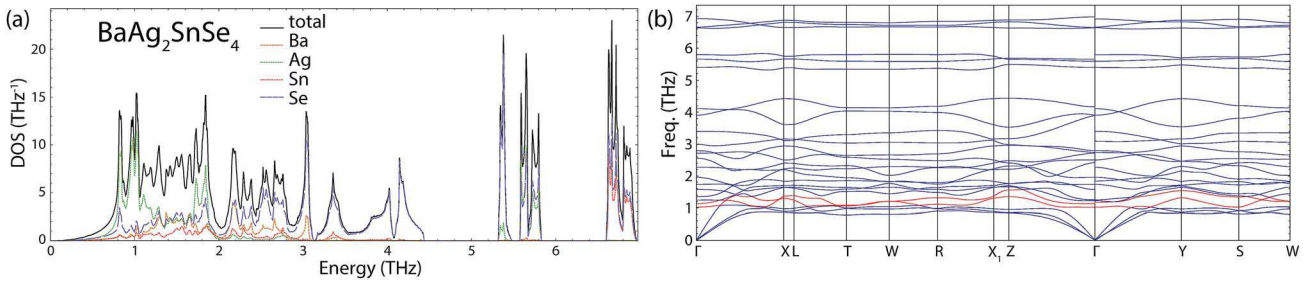

Fig. 6 Calculated phonon dispersion and phonon density of states per unit cell of $BaAg_2SnSe_4$. Hybridization of the two lowest frequency optical modes (*i.e.*, the red lines) with acoustic modes results in large Ag partial DOS in the 0.7–1 THz region. See Fig. S2† for results of $BaCu_2GeSe_4$, $BaCu_2SnSe_4$, and $SrCu_2GeSe_4$.

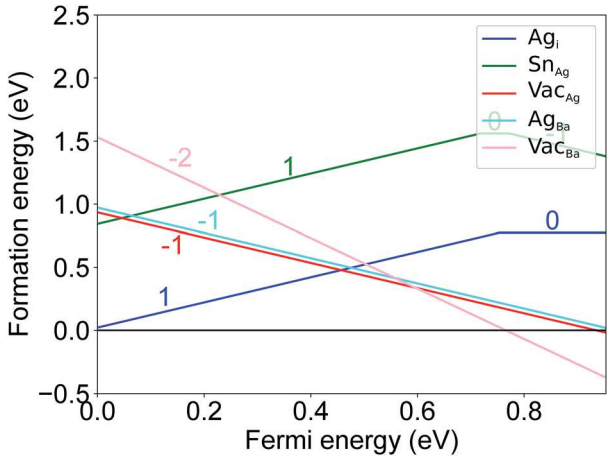

Fig. 7 HSE refinement of intrinsic defect formation energy diagram of $BaAg_2SnSe_4$. The phase region is Ba_2SnSe_5–$BaAg_2SnSe_4$–Se–$SnSe_2$. The positively charged Ag interstitials (Ag_i) act as hole killers near the VBM.

concentration of 10^{20} cm^{-3} and a constant relaxation time of 10^{-14} s (see Table S1 in ESI for more details†). In practice, however, optimizing the charge carrier concentration of these compounds is challenging. Fig. 5 shows electrical transport properties of $BaAg_2SnSe_4$ with both intrinsic (*i.e.*, Ba and Ag deficiency) and extrinsic (*i.e.*, Na on Ba site and In on Sn site) doping. The measured electrical conductivity and power factor are low due to the low doping efficiency (*e.g.*, carrier concentration 10^{16} cm^{-3} at room temperature).

Further calculations help understand the cause of such low doping efficiency. Note that many intrinsic defects (see section III in ESI†) are calculated for all the four compounds *via* the Perdew, Burke, and Ernzerhof generalized gradient approximation (PBE-GGA). PBE-GGA defect calculations severely underestimate the band gaps and show intrinsic defects favorable for p-type doping. To improve the accuracy, the lowest energy defects of $BaAg_2SnSe_4$ are recalculated with the hybrid functional of Heyd, Scuseria, and Ernzerhof (HSE) (see Section IV E for more details about the calculation). HSE defect calculations indicate that positively charged Ag donors act as hole killers; hence, restricting the hole concentration at such low levels (see Fig. 7). To reduce computational costs, the HSE calculations are only performed at the gamma point. Further details on defects calculations and corrections applied are available elsewhere.[23]

III. Conclusions

We confirm the low thermal conductivity of four quaternary selenides from both experimental and theoretical prospects. The low thermal conductivity can be attributed to both the structural distortion (*e.g.*, strongly at Ag site and slightly at Cu site) and the disorder induced by weakly bonding Ag–Ag/Cu–Cu dimers. On the other hand, the low electrical conductivity can be explained by the defects (*i.e.*, Ag interstitial) serving as hole killers. Despite the low thermoelectric efficiency, the materials can be potentially applied as an thermal-barrier coating.

IV. Experimental section

A. Sample preparation

Stoichiometric amounts of elements, *i.e.*, Ba shot (Sigma Aldrich, 99+%), Ag shot (Alfa Aesar, 99.999%), Sn shot (Alfa Aesar, 99.99%), Se shot (Alfa Aesar, 99.99%), Cu slug (Alfa Aesar, 99.995%), Ge shot (Alfa Aesar, 99.999%), were cut into small pieces and weighed in an Ar-filled glovebox. The elements were loaded into stainless-steel vials with stainless-steel balls inside the glove box filled with argon and then dry ball-milled in a stainless steel vial with two 1/2 inch stainless steel balls for an hour using a SPEX Sample Prep 8000 Series mixer/mill. The powder was collected and hot-pressed in high-density graphite dies with a 12 mm diameter, at a pressure of 45 MPa and at a maximum temperature of 450 K for 1 hours under constant argon flow, followed by 3 hours of cooling.

B. Sample characterization

Powder X-ray diffraction (PXRD) data were collected using a STOE STADI MP diffractometer (Cu Kα radiation) in transmission mode (for the power) and reflection mode (for the hot-pressed samples). The lattice parameter determination using α-Si as internal standard and Rietveld refinements were performed using the WinCSD program package.

C. Heat capacity

Low-temperature heat capacity from 2 K to 300 K was acquired using the relaxation micro-calorimetry method in a Physical Properties Measurement System (PPMS, from Quantum Design) under high vacuum (10^{-4} Torr). Details about the relaxation calorimetry can be found in ref. 24.

High-temperature heat capacity was measured *via* the enthalpic method using a TA Instruments™ Q200 differential scanning calorimeter (DSC). For the heat capacity measurement, 10 K intervals were recorded in the temperature range from 320 K to 680 K using a scanning rate of 1 K min^{-1}. Prior to and after each temperature step, the calorimeter was held isothermally for 5 min. Three runs were acquired where in the first run a hermetically sealed aluminium pan was measured to determine the background of the aluminium pans. In the second and third runs, an Al_2O_3 crystal as a standard sample and the samples, all hermetically sealed in aluminium pans, were recorded. For each temperature interval the heat flow of the background was subtracted from the heat flows of the hermetically sealed Al_2O_3, and investigated samples, respectively, using the mass ratio of the aluminium pans and the resulting heat flows were integrated over time. The heat capacity of the sample was calculated from

$$C_{p,sample} = \frac{F(\Delta\dot{Q},t)_{sample}}{F(\Delta\dot{Q},t)_{Al_2O_3}} \frac{m_{Al_2O_3}}{m_{sample}} C_{p,Al_2O_3} \quad (1)$$

where $F(\Delta\dot{Q},t)_{sample}$ and $F(\Delta\dot{Q},t)_{Al_2O_3}$ are the integrated areas of the heat flow over time of the sample and Al_2O_3, respectively, m_{sample} and $m_{Al_2O_3}$ are the masses of the sample and Al_2O_3, respectively, and C_{p,Al_2O_3} is the heat capacity at constant pressure of Al_2O_3.[25] The heat capacity of the samples was calibrated to the low-temperature heat capacity. More information about the enthalpic method can be found in ref. 26.

D. Measurements of transport properties

Electrical and thermal transport properties were measured from 300 to 723 K. The electrical resistivity and Hall coefficient measurements were determined using the 4-point probe Van der Pauw technique with a 0.8 T magnetic field under high vacuum. The Seebeck coefficients of the samples were obtained using chromel-Nb thermocouples by applying a temperature gradient across the sample to oscillate between $\pm$7.5 K.

Thermal conductivity was calculated from the relation $\kappa = DdC_p$, where D is the thermal diffusivity measured with a Netzsch LFA 457 laser flash apparatus, d is the density of the material and C_p is the heat capacity at constant pressure. C_p of $BaAg_2SnSe_4$, $BaCu_2SNSe_4$ and $SrCu_2GeSe_4$ were measured (see Section IV C). For $BaCu_2GeSe_4$, the Dulong–Petit limit was used. Experimental measurements and computational calculations of the heat capacity confirm the application of Dulong–Petit limit (see Section IV C). In addition, ultrasonic measurements were performed at room temperature to obtain the longitudinal and transverse sound velocities.

E. Computational details

First-principles electronic band structure and defects calculations were computed using Vienna *Ab initio* Simulation Package (VASP).[27,28] For band structure and phonon calculations, we used Perdew–Burke–Enzerhof (PBE) generalized gradient approximation[29] (GGA) functional and projected augmented-wave[30] (PAW) method in our calculations.

The equation used to calculate defect formation enthalpies is described in the ESI.† For a more reliable defects and bulk energy calculations we employed the hybrid functional HSE06.[31] Chemical potentials were calculated based on the total energies of the corresponding entries from the Materials project database,[32] which are handled by the pymatgen tool.[33] The total energy and the potential of the charged defects are corrected by Kumagai method[34] with the dielectric constant calculated by the PBE functional. All the procedures were implemented automatically in the pycdt code.[23]

The electrical conductivity and Seebeck coefficient were calculated using the PBE band structure and the BoltzTraP.[35] We perform such calculations with an arbitrary constant relaxation time of $\tau = 10^{-14}$ s in order to rank materials based on their predicted power factor as opposed to direct comparison with the experimental data.[36] We perform such high-throughput computations with the aid of software packages pymatgen,[33] Fireworks[37] and automate.[38]

For the calculation of Cahill–Pohl[5] minimum thermal conductivity, κ_{min}, as well as the semi-empirical[39] thermal conductivity, κ_{SE}, we calculate bulk and shear moduli from a 6 $\times$ 6 elastic tensor using the Green-Lagrange strain tensor after applying deformation to the crystal structures (details are available in ref. 40 and https://materialsproject.org/docs/calculations).

We calculate the lattice thermal conductivity from using the recently developed compressive sensing lattice dynamics (CSLD) method[19] and the second order perturbation theory combined with Boltzmann transport equation (BTE). The compressive sensing techniques[41] allows very efficient use of training supercell structures and enables us to calculate third-order force constants with relatively few first-principles calculations. Force constants are calculated using supercells with structures containing either 384 or 432 atoms with random displacement of 0.01 Å on all atoms in 4–10 supercell calculations. Then larger displacement $\approx$ 0.05 Å was adopted to calculate third-order force constants in 2–5 supercell calculations. Both second-order harmonic and third-order anharmonic interatomic force constants were extracted with the CSLD code and first-principles calculated interatomic forces of supercell structures with small displacements. The ShengBTE package[42] was used to perform iterative phonon scattering rates, lifetime and lattice thermal conductivity calculations assuming three-phonon processes. Note that our calculations of phonon scattering considering three-phonon processes likely underestimate scattering rates and overestimate lattice thermal conductivity, while four-phonon contributions are considerably more demanding[43] and are not attempted in this work.

V. Author contributions

J. J. K., U. A., A. F., A. J. and G. J. S. conceived and designed this research project; J. J. K. and U. A. carried out synthesis and transport measurements; J.-H. P. performed heat capacity measurement; F. Z. performed phonon transport calculations; G. L., A. F. and F. R. performed defect diagram calculations; J. J. K., U. A., J.-H. P., F. Z., G. I., A. F., F. R., M. A. W., G.-M. R, G. H., A. J. and G. J. S. prepared and edited the manuscript.

Conflicts of interest

There are no conflicts to declare.

Acknowledgements

JK acknowledges NSF DMREF (grant no. 1334713, 1334351, and 1333335) for support of this research. AJ and AF were funded by the U.S. Department of Energy, Office of Basic Energy Sciences, Early Career Research Program (ECRP). FZ was supported by the Laboratory Directed Research and Development program at Lawrence Livermore National Laboratory and performed under the auspices of the U.S. Department of Energy by LLNL under Contract DE-AC52-07NA27344. This research used resources of the National Energy Research Scientific Computing Center (NERSC), a DOE Office of Science User Facility supported by the Office of Science of the U.S. Department of Energy under Contract No. DE-AC02-05CH11231. JHP acknowledges support from Dalhousie Research in Energy, Advanced Materials and

Sustainability (DREAMS), an NSERC CREATE program, and a Nova Scotia scholarship. MAW acknowledges support from NSERC and the Clean Technologies Research Institute at Dalhousie University.

References

1 C. M. Bhandari and D. M. Rowe, *CRC Handbook of thermoelectrics*, CRC Press, Boca Raton, FL, 1995, p. 49.
2 S. Ohno, U. Aydemir, M. Amsler, J.-H. Pöhls, S. Chanakian, A. Zevalkink, M. A. White, S. K. Bux, C. Wolverton and G. J. Snyder, *Adv. Funct. Mater.*, 2017, **27**(20), 1606361.
3 A. Zevalkink, W. G. Zeier, G. Pomrehn, E. Schechtel, W. Tremel and G. J. Snyder, *Energy Environ. Sci.*, 2012, **5**, 9121.
4 S. R. Brown, S. M. Kauzlarich, F. Gascoin and G. J. Snyder, *Chem. Mater.*, 2006, **18**, 1873.
5 D. G. Cahill and R. O. Pohl, *Annu. Rev. Phys. Chem.*, 1988, **39**, 93.
6 C. Chiritescu, D. G. Cahill, N. Nguyen, D. Johnson, A. Bodapati, P. Keblinski and P. Zschack, *Science*, 2007, **315**, 351.
7 X. Wang, C. D. Liman, N. D. Treat, M. L. Chabinyc and D. G. Cahill, *Phys. Rev. B*, 2013, **88**, 075310.
8 Z. Guo, D. Lee, J. Strzalka, H. Gao, L. Huang, A. M. Khounsary and T. Luo, *Phys. Chem. Chem. Phys.*, 2014, **16**, 26359.
9 L.-D. Zhao, S.-H. Lo, Y. Zhang, H. Sun, G. Tan, C. Uher, C. Wolverton, V. P. Dravid and M. G. Kanatzidis, *Nature*, 2014, **508**, 373.
10 J.-H. Pöhls, A. Faghaninia, G. Petretto, U. Aydemir, F. Ricci, G. Li, M. Wood, S. Ohno, G. Hautier, G. J. Snyder, *et al.*, *J. Mater. Chem. C*, 2017, **5**, 12441.
11 J.-H. Pöhls, M. B. Johnson and M. A. White, *Phys. Chem. Chem. Phys.*, 2016, **18**, 1185.
12 M. T. Agne, R. Hanus and G. J. Snyder, *Energy Environ. Sci.*, 2018, **11**, 609.
13 F. Ricci, W. Chen, U. Aydemir, G. J. Snyder, G.-M. Rignanese, A. Jain and G. Hautier, *Sci. Data*, 2017, **4**, 170085.
14 P. Gorai, D. Gao, B. Ortiz, S. Miller, S. A. Barnett, T. Mason, Q. Lv, V. Stevanović and E. S. Toberer, *Comput. Mater. Sci.*, 2016, **112**, 368.
15 A. Assoud, N. Soheilnia and H. Kleinke, *Chem. Mater.*, 2005, **17**, 2255.
16 D. Hitchcock, Unusually Low Thermal Conductivity in the Argyrodite Ag_8GeTe_6 Attributed to Strong Anharmonicity, Doctoral Dissertation, Clemson University, 2014.
17 R. Chetty, A. Bali and R. C. Mallik, *J. Mater. Chem. C*, 2015, **3**, 12364.
18 D. G. Cahill, S. K. Watson and R. O. Pohl, *Phys. Rev. B*, 1992, **46**, 6131.
19 F. Zhou, W. Nielson, Y. Xia, V. Ozoliņš, *et al.*, *Phys. Rev. Lett.*, 2014, **113**, 185501.
20 G. J. Snyder, M. Christensen, E. Nishibori, T. Caillat and B. B. Iversen, *Nat. Mater.*, 2004, **3**, 458.
21 S. Kastbjerg, C. A. Uvarov, S. M. Kauzlarich, Y.-S. Chen, E. Nishibori, M. A. Spackman and B. B. Iversen, *Dalton Trans.*, 2012, **41**, 10347.
22 U. Aydemir, A. Zevalkink, A. Ormeci, Z. M. Gibbs, S. Bux and G. J. Snyder, *Chem. Mater.*, 2015, **27**, 1622.
23 D. Broberg, B. Medasani, N. E. Zimmermann, G. Yu, A. Canning, M. Haranczyk, M. Asta and G. Hautier, *Comput. Phys. Commun.*, 2018, **226**, 165.
24 C. A. Kennedy, M. Stancescu, R. A. Marriott and M. A. White, *Cryogenics*, 2007, **47**, 107.
25 D. G. Archer, *J. Phys. Chem. Ref. Data*, 1993, **22**, 1441.
26 S. D. Kang, J.-H. Pöhls, U. Aydemir, P. Qiu, C. C. Stoumpos, R. Hanus, M. A. White, X. Shi, L. Chen, M. G. Kanatzidis and G. J. Snyder, *Materials Today Physics*, 2017, **1**, 7.
27 G. Kresse and J. Furthmüller, *Comput. Mater. Sci.*, 1996, **6**, 15.
28 G. Kresse and J. Furthmüller, *Phys. Rev. B*, 1996, **54**, 11169.
29 J. P. Perdew, K. Burke and M. Ernzerhof, *Phys. Rev. Lett.*, 1996, **77**, 3865.
30 P. E. Blöchl, *Phys. Rev. B*, 1994, **50**, 17953.
31 J. Paier, M. Marsman, K. Hummer, G. Kresse, I. Gerber and J. Angyan, *J. Chem. Phys.*, 2006, **124**, 154709.
32 A. Jain, S. P. Ong, G. Hautier, W. Chen, W. D. Richards, S. Dacek, S. Cholia, D. Gunter, D. Skinner, G. Ceder, *et al.*, *APL Mater.*, 2013, **1**, 011002.
33 S. P. Ong, W. D. Richards, A. Jain, G. Hautier, M. Kocher, S. Cholia, D. Gunter, V. L. Chevrier, K. A. Persson and G. Ceder, *Comput. Mater. Sci.*, 2013, **68**, 314.
34 Y. Kumagai and F. Oba, *Phys. Rev. B*, 2014, **89**, 195205.
35 G. K. Madsen and D. J. Singh, *Comput. Phys. Commun.*, 2006, **175**, 67.
36 W. Chen, J.-H. Pöhls, G. Hautier, D. Broberg, S. Bajaj, U. Aydemir, Z. M. Gibbs, H. Zhu, M. Asta, G. J. Snyder, *et al.*, *J. Mater. Chem. C*, 2016, **4**, 4414.
37 A. Jain, S. P. Ong, W. Chen, B. Medasani, X. Qu, M. Kocher, M. Brafman, G. Petretto, G.-M. Rignanese, G. Hautier, D. Gunter and K. A. Persson, *Concurrency and Computation: Practice and Experience*, vol. 27, pp. 5037, 2015.
38 K. Mathew, J. H. Montoya, A. Faghaninia, S. Dwarakanath, M. Aykol, H. Tang, I. heng Chu, T. Smidt, B. Bocklund, M. Horton, J. Dagdelen, B. Wood, Z.-K. Liu, J. Neaton, S. P. Ong, K. Persson and A. Jain, *Comput. Mater. Sci.*, 2017, **139**, 140.
39 S. A. Miller, P. Gorai, B. R. Ortiz, A. Goyal, D. Gao, S. A. Barnett, T. O. Mason, G. J. Snyder, Q. Lv, V. Stevanovic and E. S. Toberer, *Chem. Mater.*, 2017, **29**, 2494.
40 M. De Jong, W. Chen, T. Angsten, A. Jain, R. Notestine, A. Gamst, M. Sluiter, C. K. Ande, S. Van Der Zwaag, J. J. Plata, *et al.*, *Sci. Data*, 2015, **2**, 150009.
41 E. J. Candès and M. B. Wakin, *IEEE Signal Processing Magazine*, 2008, **25**, 21.
42 W. Li, J. Carrete, N. A. Katcho and N. Mingo, *Comput. Phys. Commun.*, 2014, **185**, 1747.
43 T. Feng and X. Ruan, *Phys. Rev. B*, 2016, **93**, 045202.

